Renewable Energy 156 (2020) 913–930

Contents lists available at ScienceDirect

Renewable Energy

journal homepage: www.elsevier.com/locate/renene

The development, design and characterisation of a scale model Horizontal Axis Tidal Turbine for dynamic load quantification

Matthew Allmark [a, *], Robert Ellis [a], Catherine Lloyd [a], Stephanie Ordonez-Sanchez [b], Kate Johannesen [b], Carl Byrne [a], Cameron Johnstone [b], Tim O'Doherty [a], Allan Mason-Jones [a]

[a] Cardiff University School of Engineering, Cardiff, CF24 3AA, United Kingdom
[b] Department of Mechanical and Aerospace Engineering University of Strathclyde, James Weir Building, Level 8, 75 Montrose Street, Glasgow, G1 1XJ, United Kingdom

ARTICLE INFO

Article history:
Received 12 June 2019
Received in revised form
25 March 2020
Accepted 10 April 2020
Available online 26 April 2020

Keywords:
Horizontal axis tidal turbine
Scale turbine development
Computational fluid dynamics
ANSYS CFX
Turbine characterisation

ABSTRACT

The paper describes the development and characterisation of three 0.9 m diameter lab-scale Horizontal Axis Tidal Turbines. The blade development process has been outlined and was used to generate a design specification. Each turbine houses instrumentation to measure rotor thrust, torque and blade root bending moments on each blade, in both 'flapwise' and 'edgewise' directions. A permanent magnet synchronous machine and encoder are integrated to allow for servo-control of the turbine as well as to provide position and rotational velocity measurements, resulting in three turbines that can be individually controlled using speed or torque control. Analogue signals are captured via a real-time operating system and field programmable gate array hardware architecture facilitating sample rates of up to 2 kHz. Results from testing the pilot turbine at three differing facilities during the development process are presented. Here good agreement, less than 7% variation, was found when comparing the testing undertaken at various flume and tow tank facilities. Lastly, the findings of a test campaign to characterise the performance of each of the three turbines are presented. Very good agreement in non-dimensional values for each of the three manufactured turbines was found.

© 2020 The Authors. Published by Elsevier Ltd. This is an open access article under the CC BY license (http://creativecommons.org/licenses/by/4.0/).

1. Introduction

Energy extraction from the ocean's tides has gained widespread acceptance as a potential contributor to the UK energy mix [1]. Increased interest in tidal energy extraction has, in part, been driven by the realisation of finite global resources and environmental impacts of burning fossil fuels [2]. The EU Renewable Energy Directive has recently extended previous commitments to stipulate that the EU community will fulfil 35% of its energy needs via updated citataionrenewable sources by 2030; it is foreseen that tidal energy extraction could go some way to helping achieve this target [3].

In order for Horizontal Axis Tidal Turbine (HATT) devices to generate energy at a competitive levelized cost of energy (LCOE), effective strategies for reducing device over-engineering and the burden of operation and maintenance costs are required. In order to achieve the 20 year lifespan [4] - quoted as being required for cost effective energy extraction - whilst reducing device over engineering, detailed understanding of HATT operational loads is required. Knowledge of normal operational loads, extreme operational loads and the characteristics of load fluctuations is required to minimise the probability of device failure due to overloading and fatigue.

During the projected turbine life cycle, extreme loads can arise from current-wave interactions, from flow acceleration around upstream turbines and from high speed turbulent structures in the on-coming fluid flow. Furthermore, these loads sources, as well as the effects of tidal cycles and turbine rotation, lead to a variety of cyclic loading events at various magnitudes and frequencies. In moving towards robust and cost effective designs, understanding and quantification of these loads will be required. It would seem

* Corresponding author.
E-mail addresses: AllmarkMJ1@cardiff.ac.uk (M. Allmark), EllisR10@cardiff.ac.uk (R. Ellis), LloydC11@cf.ac.uk (C. Lloyd), s.ordonez@strath.ac.uk (S. Ordonez-Sanchez), kate.porter.10@alumni.ucl.ac.uk (K. Johannesen), byrne@cardiff.ac.uk (C. Byrne), cameron.johnstone@strath.ac.uk (C. Johnstone), Odoherty@cardiff.ac.uk (T. O'Doherty), mason-jonesA@cardiff.ac.uk (A. Mason-Jones).

https://doi.org/10.1016/j.renene.2020.04.060
0960-1481/© 2020 The Authors. Published by Elsevier Ltd. This is an open access article under the CC BY license (http://creativecommons.org/licenses/by/4.0/).

pertinent to develop a series of standard load specifications under a number of operational and environmental scenarios to which turbines can be designed and ultimately 'signed-off' against - similar to the IEC 61400 standard for the wind industry [5]. Although difficulties in adapting such an approach to the tidal industry surely exist, such a methodology will allow for increased load understanding, design maturity and improved turbine life expectancy forecasting. Developments in the above are likely to bolster investor confidence and will aid in device underwriting by insurance companies - two important aspects that need to be addressed in order to create a functioning industry for the future.

This paper outlines the development process undertaken in designing and manufacturing three instrumented 1/20th scale HATT devices in order to understand the dynamic loading of HATTs, to inform developers and help achieve survivability and efficiencies in the marine energy sector. The three devices have been manufactured and used for testing of HATTs singularly as well as in array configurations. In this way the impacts of array operation and structure on turbine loading can be studied at scale. The paper describes the design specification, testing of the three HATTs at three separate test facilities (the Consiglio Nazionale delle Ricerche Institute of Marine Engineering (CNR-INM) wave-tow tank, the Institut Francais de Recherche pour l'exploitation de la mer (IFREMER) re-circulating flume and the Kelvin Hydrodynamic Laboratory (KHL) tow tank) to characterise each turbine individually against the specifications. The individual data outputs were then compared to check for consistency. Initially the results relating to a single turbine undergoing testing at the CNR-INM facility are presented, this followed by a comparison of the outputs of the three turbines recorded at KHL. Lastly, a detailed analysis of the turbine performance at the IFREMER flume is presented considering the repeatability of the turbine measurements, the dimensional power and thrust performance, the drive shaft losses and Reynolds effects associated with turbine operation under low turbulence intensity flow regimes.

2. A review of lab-scale turbine testing and design

For the last 15–20 years, testing and development of scale model turbines has been utilised in both research and by turbine developers [6–12]. Scale model testing has allowed developers to further understand design decisions during early Technology Readiness Levels (TRLs) with relatively small investments needed. In terms of research, the use of scale model HATTs has proliferated and allowed researchers to understand the fundamental fluid dynamics, loading mechanisms and efficiencies associated with a variety of HATT rotor configurations. Furthermore, scale model testing has formed a vital part of using numerical modelling techniques to inform design modifications, both economically and relatively quickly, by providing validation data. Generally, scale testing to-date has proceeded at the 1/30th or higher depending on the size of the test facilities available for testing such devices. The use of nursery sites, however, has allowed for the development and testing of 1/5th scale devices - which is often a crucial step in moving towards a higher TRL full-scale deployments. As the turbine development detailed within this paper is specific to a 1/20th scale HATT this review section will be constrained to consider the form case exclusively.

In terms of first-hand experience gained by the authors, Cardiff Marine Energy Research Group (CMERG) has previously developed three working 0.5 m diameter turbines. These have been used to conduct turbine design studies using CFD. Both turbines were developed using the HATT form. Details of the first turbine arrangement can be found in Ref. [13]. Testing with the first generation turbine was successful in validating and informing CFD models developed within the research group. The second generation lab-scale HATT was also developed, details of which are outlined in Ref. [14,15]. The turbine rotor and braking motor were directly coupled via a short drive shaft. This required that the motor was mounted inside the turbine housing, i.e. in the manner that is similar to many commercial turbine set ups with the motor taking the position of a Permanent Magnet Synchronous Machine (PMSM - typically used for direct drive applications). Thrust on the turbine structure, including the stanchion was measured. This turbine was used extensively in studying the power converted and wake recovery associated with the rotor under plug flows, profiled flows, flow misalignment, wave current interaction and blade fault diagnostics Citations improved as suggested [13–18]. A third generation turbine was then designed within CMERG. The turbine was created using a similar rotor setup to the previous model scale allowing for both speed and torque control of the turbine. The turbine was fitted with a thrust and twisting moment transducer for a single blade, as well as an accelerometer housed in the nose cone. The rotor data captured was logged remotely via an Arduino mounted in the turbine nose cone. A similar stanchion arrangement was used to measure thrust loading on the turbine. The torque developed via the turbine rotor was measured via the integrated PMSM. This generation HATT was used for a variety of test campaigns studying turbine rotor faults, the effect of turbine yaw angle, wave loading effects and bend-twist coupling for blade load shedding Citations improved as suggested [13–19].

3. Blade design

The blade, and ultimately the rotor, design of the detailed lab-scale device was developed to allow for adherence to Reynolds scaling and preservation of the Kinematic relationship between the blade tip speed relative to the incident fluid velocity. Details on the approach to Reynolds scaling can be found [20]. The Wortmann FX63-137 aerofoil has been used by CMERG for producing scaled HATT blades. Initially designed by Egarr [21], the blades have been extensively tested both numerically and experimentally [13,15]. The aerofoil has high lift and low stall characteristics and a large root chord length which aids a self starting capability [4]. An important aspect of the design and development of the turbine was the development of an optimised turbine rotor based on the Wortmann FX63-137 aerofoil. The chord lengths, twist distribution from root to tip, pitch angle and hub attachment method were all studied, with the goal of increasing the power coefficient, Cp, from a peak of 0.4 while maintaining the thrust coefficient, C_T, to within 10% of the levels observed in the previous blade geometry (i.e. $C_T \approx 0.88$ at Peak C_P and ≈ 0.99 at freewheeling).

To aid the development of the rotor and turbine specification, the non-dimensional coefficients have been utilised and defined by Equations (1)–(4), below. Dimensional data have, however, been used where appropriate and specified along with a reference fluid velocity.

$$C_P(\lambda) = \frac{Power}{0.5\rho A V^3} \tag{1}$$

$$C_\theta(\lambda) = \frac{Torque}{0.5\rho A R V^2} \tag{2}$$

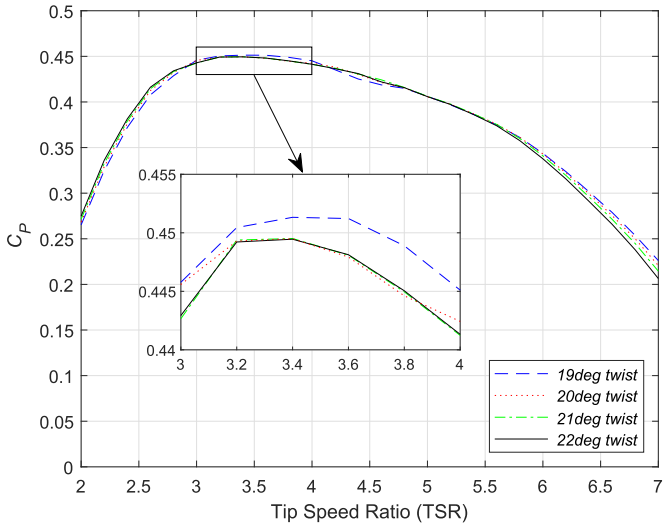

Fig. 1. Comparison of the BEMT C_P predictions for twist distributions between 19 and 22°..

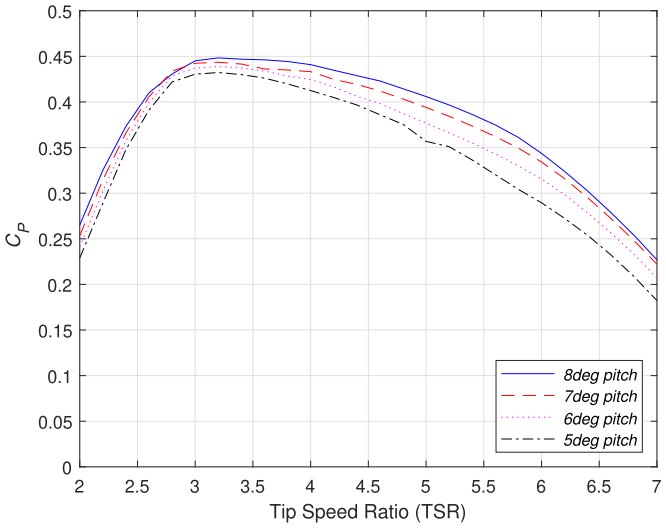

Fig. 2. Comparison of the BEMT C_P predictions for pitch angles of 5–8°..

$$C_t(\lambda) = \frac{Thrust}{0.5\rho A V^2} \tag{3}$$

where the tip speed ratio (λ), is given as,

$$\lambda = \frac{\omega R}{V} \tag{4}$$

where, V is the fluid velocity in ms^{-1}, ρ is the density of water in kg/m^3, A is the turbine swept area in m^2, R is the turbine radius in m and ω is the rotational velocity in $rads^{-1}$. The two methods used for the design development were Blade Element Momentum Theorem (BEMT)and Computational Fluid Dynamics (CFD).

3.1. Blade element momentum theory

Optimising the blade design based on the Wortmann FX 63–137 profile was conducted in two stages: 1) the chord length distribution from blade root to tip and 2) the blade twist distribution. In total over 130 variations were considered using the University of Strathclyde BEMT code [22]. One of the main reasons for using BEMT initially is that the execution and compilation of the code is comparatively simple, when compared to other numerical methods and the blade design can be produced quickly, allowing for the efficient study of a large number of blade geometry cases as required. The lift and drag coefficients for the Wortmann aerofoil were calculated using XFoil. The C_P and C_T were compared for various chord length and twist distributions. Those designs with the highest performance coefficients were plotted and the peak C_P was just over 0.45 at $\lambda \approx 3.5$, was found to be for a 19deg twist, as shown in Fig. 1.

Finally a range of pitch angles between $5^o - 8^o$ were studied in more detail. C_P and C_T, for these pitch angles, can be seen in Figs. 2 and 3, respectively. The pitch angle of 8^o was found to yield the highest $C_P \approx 0.45$ with a $C_T \approx 0.88$ at $\lambda \approx 3.5$.

3.2. Computational Fluid Dynamics

The optimised geometry, with a 384.5 mm blade length, was modelled using ANSYS CFX. Approximately, 60 mm length of the blade, from the root, was modified and blended with the

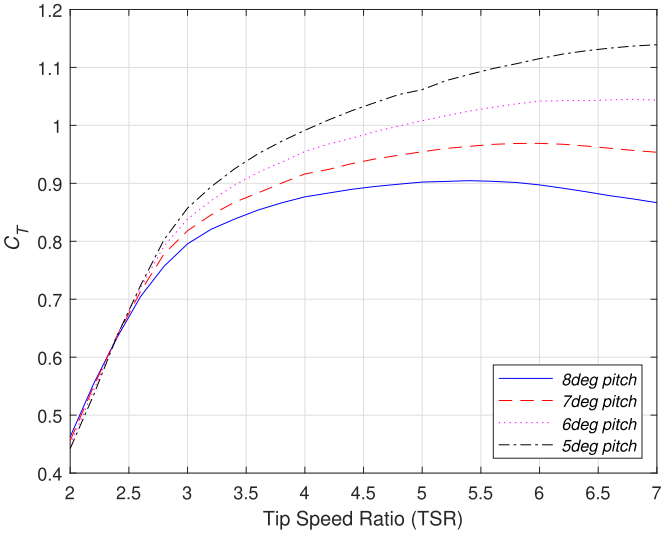

Fig. 3. Comparison of the BEMT C_T predictions for pitch angles of 5–8°.

Wortmann profile to enable the blade to be connected to the turbine hub. The models developed all contained a Moving Reference Frame (MRF), as sub domain which encompassed the entire turbine rotor. The inclusion of the MRF facilitated simulation of the turbine rotation. The width, depth and height of the overall fluid domains were generated to replicate the geometries of the test facilities ultimately used for turbine characterisation.

An outline of the CFD models are presented here, with details presented in Table 1. However, further details can be found in Ref. [23]. Each blade was divided into three sections: the blade tip, middle and root. The smallest elements were concentrated at the tip, starting at 3 mm gradually increasing to 7 mm at the root and hub. The growth rate, specifying the rate of cell size growth, was set to 1.1, with the maximum element size set to 20 mm, which resulted in 3 million elements, with around half of these elements contained within the MRF. A 1 ms^{-1} plug flow boundary condition was applied to the inlet of the model domain and a static pressure of 0 Pa at the outlet. The walls, base, faces of

Table 1
CFD modelling information.

Model Name		No Stanchion	CNR-INM	IFREMER
Geometry	Domain Dimensions	6[m] x 6[m] x 11[m]	9[m] x 3.5[m] x 20[m]	4[m] x 2[m] x 18[m]
	Stanchion	No	Yes	Yes
Set Up	Inlet	1[m/s]	1[m/s]	1.1[m/s]
	Outlet	Pressure 0[Pa]	Pressure 0[Pa]	Pressure 0[Pa]
	Walls	Free Slip	No Slip	No Slip
	Top	Free Slip	Opening	Opening
	Solver Type	Steady	Steady	Steady

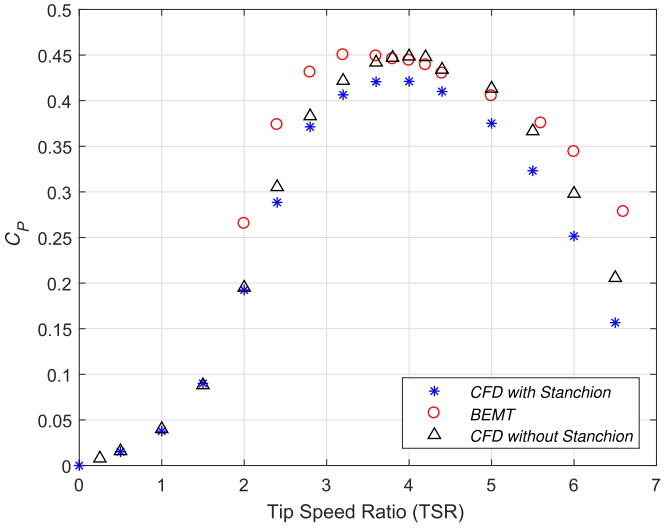

Fig. 4. *Comparison of the C_P between CFD and BEMT.*

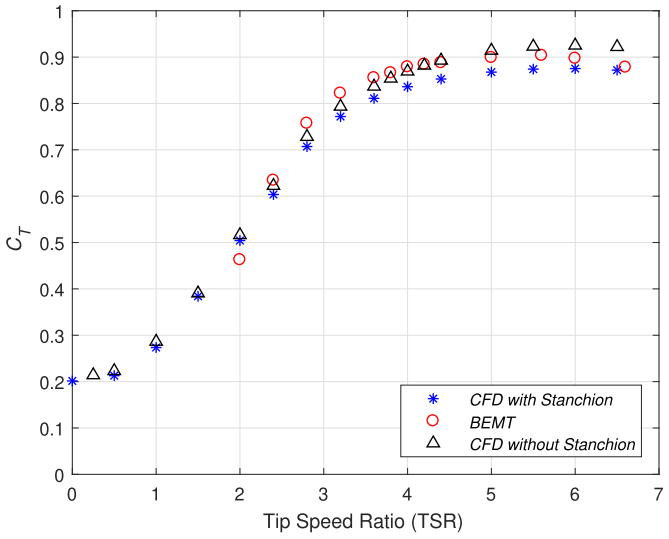

Fig. 5. *Comparison of the C_T between CFD and BEMT.*

turbine, hub and stanchion were all set to the no slip condition with the top of the domain defined as an opening. The RANS equations were closed using the SST k-ω turbulence model as developed by Ref. [24] and successfully applied to tidal turbine modelling in Ref. [13,15,16,20]. A comparison made between the torque and thrust results from the steady state and transient models showed less than 2% differences hence the steady state model was used to reduce modelling time.

The results from the CFD modelling along with the BEMT results are presented in Figs. 4 and 5, with the final rotor parameters presented in Table 2. By comparing the BEMT to the CFD model that includes the stanchion it can be seen that the BEMT generates higher predictions for both the C_P and C_T, due to the stanchion not being taken into consideration as part of the BEMT calculation. The flow directly behind the blades will have a lower velocity due to the blockage effect of the stanchion and ultimately reduce the performance of the blade passing the stanchion [15]. If the stanchion is removed from the CFD model and compared with the BEMT results, then a much closer comparison between both the thrust and the power can be seen.The BEMT results also showed a lower λ value for peak power. The authors suggest that this may be due to Reynolds effects in matching the lift and drag coefficients, similar findings were presented in Ref. [25]. Experimental results showing the effect of Reynolds Number on turbine performance can be found in Appendix A and are show in.Fig. A19..

Table 2
Overview of new rotor ($D = 0.9m$) parameters used to develop the design specification.

Quantity	Rotor Value
Peak C_P	0.42 ($\lambda \approx 4.0$)
Peak C_T	0.88 ($\lambda \approx 6.0$)
Peak C_q	0.14 ($\lambda \approx 2.0$)
Freewheeling	$\lambda = 8$
Peak Power	293 W (110*RPM*)
Peak Thrust ($U = 1.3ms^{-1}$)	615 N (165*RPM*)
Peak Torque ($U = 1.3ms^{-1}$)	44 Nm (55*RPM*)
Max RPM at $1.3ms^{-1}$	220

4. Turbine design

The following section details the design of the nacelle, drive train, electronic machine and instrumentation generated to compliment the newly developed blades forming a 1/20th instrumented HATT. The section is split into two parts. The first focusses on the design requirements for the turbine development and the second details the design solution developed to meet the outlined requirements.

4.1. Design criteria

The specifications for the turbines are shown in Table 3A. The C_T and C_P for the rotor geometry were used to develop the rated loadings and power output for the HATT design. As the CFD

Table 3
Table outlining the main design specifications and Instrumentation List for the developed HATT.

A.	
Requirements List	
Specification	Details
Rated Flow Velocity	Continuous: 1.3 ms^{-1} Instantaneous: 1.5 ms^{-1}
Rated Power	0.6 kW
Maximum Rotational Velocity	350 RPM
Rated Torque	Continuous: 41 Nm Instantaneous: 54 Nm
Maximum Rotor Thrust	1.07 kN
Maximum Blade Root Bending Moment	Flapwise: 129.76 Nm Edgewise: 18.13 Nm
Sample Rate	1032 Hz
Load Measurements	
Control Types	Speed Control (SC), Torque Control (TC) Regulated Torque Control Optimal λ control
B.	
Instrumentation List	
Flap-wise and Edge-wise blade root bending moments (each blade); Rotor Thrust; Rotor Torque; Rotor Position; Rotational Velocity; PMSM Torque; Stanchion Bending Moment; Support Structure Vibration.	

results hadn't been validated at this stage, a safety factor of 1.5 was applied to the rated quantities, at a mean flow velocity of 1.3 ms^{-1} and instantaneous velocities up to 1.5 ms^{-1} (based on a turbulence intensity of 15%). This corresponds to a mean chord based Reynolds number, $RE_{0.7Chord} = 8.44E + 4$ as defined in A. The design loads were based on the standard equations defined in Equations (1)–(4).

The diameter of the turbine was specified as 0.9m, this was in line with a 1/20th scale HATT. A direct-drive device was decided upon, this was based upon the experience acquired during development of the legacy HATTs developed by the authors and detailed in Ref. [14]. The turbine control and power take-off were to be undertaken by a PMSM. The power flow from the turbine and its associated braking torque were to be controlled by a drive series made up of back-to-back Voltage Source Converters (VSCs) either side of a DC bus. This decision was made based on the flexibility demonstrated when previously using such a set up. Previously closed-loop, set-point speed and torque control had been demonstrated. Furthermore, with the addition of outer control loops this set up could be utilised to achieve optimal power and torque control strategies allowing for more focused research into turbine loadings under representative control scenarios [26].

As the primary aim of the scale model HATT was for use in studying dynamic and transient loading characteristics, rotor load measuring instrumentation was to be included. This ensured that the turbine was capable of providing dynamic, C_P, C_T and C_θ measurements directly associated with the turbine rotor. To compliment this the capability of measuring the dynamic blade root bending moments, for each turbine blade, was incorporated. To allow for the high fidelity study of transient loading throughout a turbine rotation, sample rates were required such that one sample per 2° was collected at turbine free-wheeling for the rated fluid velocity of 1.3 ms^{-1}. Based on the power curves developed via CFD, free-wheeling was found to occur at, $\lambda \approx 8$. At 1.3 ms^{-1} this corresponds to a free-wheeling rotational velocity of 220 RPM or a sampling rate of 1324 Hz to fulfil the stipulated requirement. Lastly, the requirement was stipulated of a maximum measurement uncertainty (for each instrument) of 5 % of the maximum loads measured for each instrument.

4.2. Design overview

A cross section of the turbine can be seen in the rendered SolidWorks image shown in Fig. 6. The HATT power transfer mechanism utilises a direct-drive set-up with turbine control and power take-off undertaken by a Permanent Magnet Synchronous Machine (PMSM) controlled via back-to-back VSCs. The front section of the turbine was developed to house an instrumentation suite consisting of an integrated rotor thrust/torque transducer, an encoder and an instrumented rotor. The instrumented rotor was developed to measure, 'flap-wise' and 'edge-wise' blade root bending moments for each turbine blade.

Additional installed instrumentation includes a moisture sensor, stanchion bending moment measurements and support structure vibration measurements. The instrumentation wiring is transferred into the rotational reference frame by an 18-way slip ring mounted on the turbine drive shaft. The turbine body is flanged together with the support stanchion through which the power, encoder and instrumentation cables are fed.

4.3. Drive train design

The turbine was designed as a direct drive HATT. As shown in Fig. 6, it was created via two drive interfacing shafts to allow for the flanging arrangement to the thrust/torque transducer. Using two drive shafts also facilitated the positioning of the PMSM on back side of the turbine away from the rotor instrumentation. The structure of the design was created to introduce modularity into the design to allow for instrumentation developments and ease of part replacement. The design decision to position the PMSM at the back end of the HATT was also undertaken to reduce electrical noise in the measurement readings.

The drive shaft was supported by three bearing housings; the mid support, front and back plates. The first shaft has a hollowed section to accommodate instrumentation cabling, which was fed from the rotating portion of the 18-way slip ring. The front shaft was supported by double row bearings, which act as the main thrust bearing and are housed in the front plate. A dynamic seal was embedded in the front plate to protect from water ingress.

The main drive shaft was supported in two places, at the mid

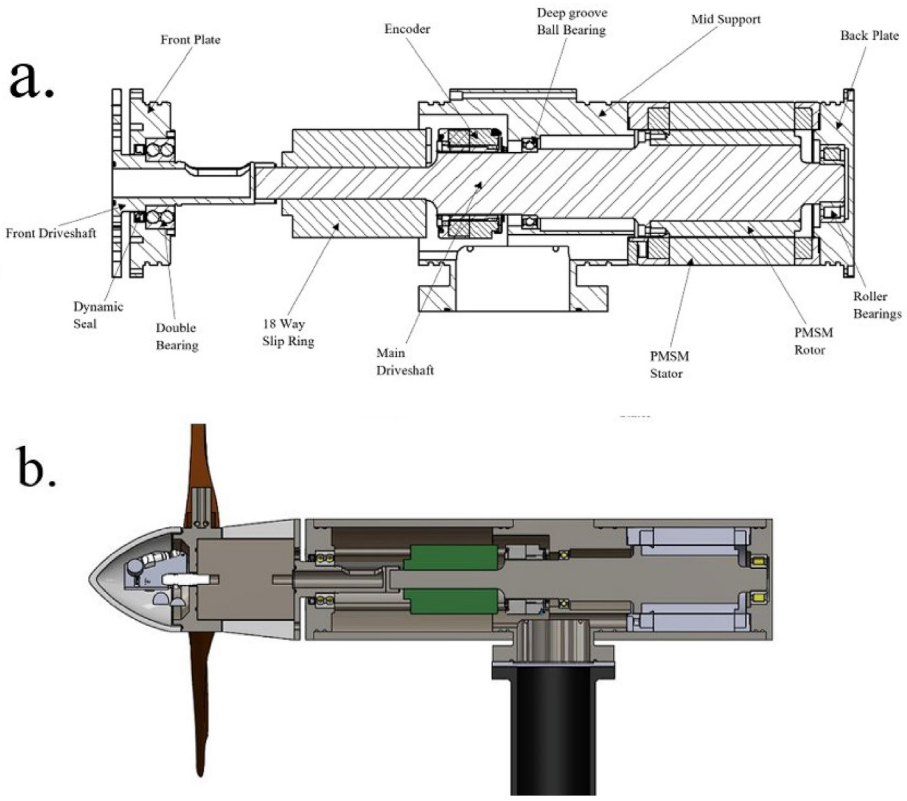

Fig. 6. Solidworks rendering of the 1/20th scale HATT.

Table 4
The motor parameters for the Bosch Rexroth MST130E.

Motor Parameters	
Rated Torque	42 Nm
Maximum Speed	350 RPM
Rated Power	0.6 kW
Maximum Rotational Velocity	350 RPM
No. of Pole Pairs	10
Winding Resistance	14.9 Ω
Mass of Stator	7.7 kg
Mass of Rotor	2.2 kg

support and back plate. The front and back drive shafts are coupled together to transfer torsional loads and rotational motion. The main shaft has been fitted with an encoder and slip ring to the left of the mid plate and a PMSM to the right of the mid plate with respect to Fig. 6.

4.4. Permanent magnet synchronous machine, drives and control

The model scale HATT houses an embedded PMSM for turbine breaking and control. The PMSM used was a Bosch Rexroth MST 130E. The ratings of the motor are presented in Table 4. The motor was chosen for its relative high torque capacity for a non-directly cooled motor as required by the direct-drive configuration. The rotor of the PMSM houses permanent magnets arranged into 10 pole pairs and was mounted on the back drive shaft fastened via a flange. The stator contains the motor windings and was integrated via the mid-section and back plates of the HATT. To cool the motor appropriately, the motor was aligned and fitted into the stainless steel nacelle of the HATT. Circular steps on the mid-section and back plate align the stator relative to the drive shaft to preserve the air gap of 0.4 mm.

Power flow to and from the PMSM was managed by a drive section, which was located in a cooled drive cabinet. The drive sections are made up of a mains choke, a mains filter, a rectifier and an inverter. A three phase connection was made to the mains choke which manages regenerative energy feedback into the grid when required. The three phase connection was the made between the mains choke and the mains filter, filtering was undertaken to maintain power quality in the supply to the rectifier. The filtered three phase connection was then fed to a rectifier where the AC current was converter to DC via a VSC with a switching frequency of 4000 Hz. The rectifier and inverter are connected via a DC bus integrated with a DC bus capacitor. The inverter then creates a three phase AC current which was

connected to the motor. The power flow to and from the motor are managed by the VSCs either side of the DC bus - similar to back-to-back set up used for HATTs and wind turbines adopting a direct-drive PMSM topology. The back-to-back VSCs allow for servo based Vector Oriented control of the turbine to directly the torque required of the PMSM or via an additional velocity control loop the desired rotational velocity. The encoder required for servo-control of the PMSM is detailed in Section 4.5.3.

4.5. Instrumentation

An instrumentation suite was integrated into the turbine in order to quantify dynamic loadings on the HATT under various fluid flow regimes. An overview of the instrumentation suite integrated into the turbine is presented below. Appendix B presents an overview of the instrument calibration process and reports the uncertainty associated with measured quanities. Figs. B20 and B21 and Tables B9 to B12 show the relevant data.

4.5.1. Rotor torque and thrust transducer

A bespoke rotor torque and thrust transducer was created by Applied measurements Ltd. The transducer used was an adapted DBBSS/TSF Torque and Axial Force Sensor, which had a rated maximum thrust load of 1.8 kN and a maximum rated torsional loading of 100 Nm. The transducer was adapted for the specified load rating, for waterproofing, to house two 18 way Lemo EGG.2B.318 connectors and to accommodate through wiring for hub instrumentation. The transducer was fastened between the front drive shaft and the turbine rotor upstream of any bearings or seals to measure rotor loads prior to any drive shaft losses. The transducer used two ICA4H amplifiers, one for thrust loading with a sensitivity of 0.005 mA/N and one for torque loading with a sensitivity of 0.08 mA/N, both amplifiers were housed in the body of the transducer.

4.5.2. Instrumented hub

The turbine hub was created to house the blades and measure both flap-wise and edge-wise bending moments on each of the three turbine blades. The hub is a circular section with holes for flange fixing to the thrust/torque transducer, a bore in the centre accommodates a Lemo connector for instrumentation wiring. Three 'bosses' project radially from the outside of the circular section, to which the blades are attached via grub screws. Each of the bosses were spaced at 120° and each of the bosses houses two full-bridge strain gauge set ups for measuring blade root bending moments.

The boss sizes were set such that they limited the stress on the machined faces to 30% of the material yield stress, whilst setting a suitable strain level on the faces.

4.5.3. Encoder

The encoder selected, and used for position feedback, was an optical encoder, the model utilised was the Heidenhain ENC113 encoder with Endat 2.2 interfacing. The encoder is of 13 bit type with a quoted system accuracy of ± 20 s of arc.

4.5.4. Amplification and signal processing

The blade load and thrust/torque transducer measurements all utilised integrated circuit ICA4H amplifiers. The output of the amplifiers was between 4 mA and 20 mA and can accommodate bridge systems with sensitivities between 0.5 mV/V and 150 mV/V. A gain setting resistor was used to achieve measurements in the 4 mA–20 mA range for differing bridge sensitivities. The amplifier required 24 V input and outputs a regulated 5 V supply to the wheatstone bridge configurations. The amplifier has an inbuilt low-pass filter with a fixed cut-off frequency of 1 kHz.

The stanchion bending moment instrumentation, consisting of a full-bridge configuration of strain gauges, was amplified and filtered by a PCM Strain Gauge Amplifier(SGA). The PCM SGA was set to filter the amplifier output at 1 kHz. Lastly, the piezo-electric vibration sensors signals are not amplified and are filtered at the NI9234 DAQ card by a low pass filter with the cut-off frequency set to set to 5 kHz. The low pass filters cut-off values are set to act as an anti-aliasing filter to ensure quality of transient analysis of the captured loading and vibration data. Table 5 shows the sample rate and anti-aliasing filter cut-off frequency for each piece of instrumentation.

4.5.5. Data acquisition

Data acquisition for all three turbines was undertaken via a National Instruments Compact RIO. The DAQ cards used in the compact RIO are outlined in Table 5. The table shows the measurement type, bit depth, sample rate and anti-aliasing filter cut-off frequency for each of the channels. A Compact RIO was utilised due to the advantages of being able to utilise both the Field Programmable Gate Array (FPGA) and the Real-Time operating system for test control and data capture and management. The tasks undertaken by the Compact RIO have been broadly split into data capture and triggering, which was undertaken by the FPGA and data management and test control which was undertaken by the Real-Time operating system.

4.6. Waterproofing and moisture sensor

Fig. 7 shows an overview of the sealing arrangement for the main turbine assembly. Generally, sealing of the turbine was accomplished using O-rings, with O-ring sizing and groove specification undertaken following the BSI 4518 British standard. As mentioned a dynamic seal was utilised to seal around the entry

Table 5
Table outlining the NI DAQ cards used for data capture along with information on the measurement type, bit depth, sample rate and anti-aliasing filter cut-off frequency.

Measurement Type	DAQ Card	Bit Depth	Sample Rate	Low Pass Cut-off
Blade root bending moment	NI9203	16-Bit, 0–20 mA	2 kHz	1 kHz
Rotor Thrust	NI9203	16-Bit, 0–20 mA	2 kHz	1 kHz
Rotor Torque	NI9203	16-Bit, 0–20 mA	2 kHz	1 kHz
Stanchion Bending Moment	NI9207	24-Bit, 0–10 V	2 kHz	1 kHz
Stanchion Vibration	NI9234	24-Bit, 0–100 mV	10 kHz	5 kHz

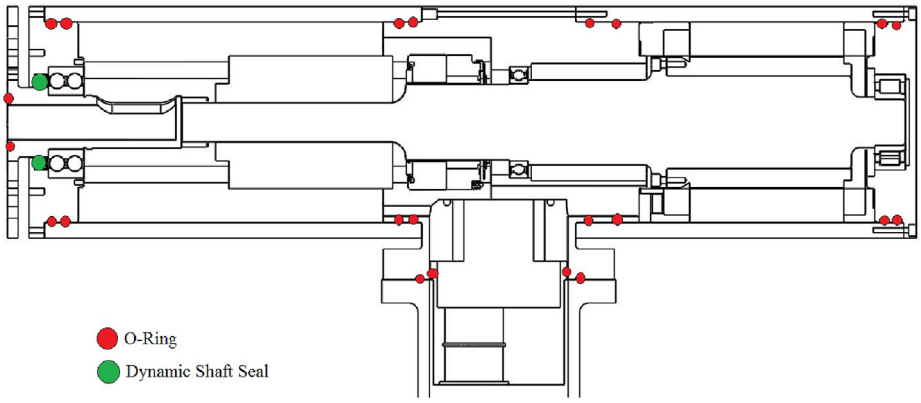

Fig. 7. Overview of the sealing arrangements for the 1/20th Scale HATT.

point of the front drive shaft into the turbine nacelle through the front plate.

An interlock moisture sensor was integrated into the turbine to alert the user in the event that any of the outlined sealing arrangements failed and water ingress into the turbine occurred. This feature was required for both safety and to protect the scale model HATT hardware. The circuit was connected to 10 V source, output from the Compact RIO; in the event of water ingress the two moisture probes are shorted or connected together. The shorting of the two probes changes the circuit output from 10 V to 0V (ground). A 0 V reading from the moisture sensor then starts an automatic shut down of the turbine PMSM to avoid any electrical damage. Lastly, the user would be alerted of the leak so the turbine can be removed from the tow tank or flume.

5. Turbine characterisation testing

Initially, a single turbine, Turbine T1, was manufactured and tested. Once this turbine was validated in terms of design and operation the further two turbines, T2 and T3, were constructed. As such, turbine testing was conducted in 3 stages:

Stage 1: Testing undertaken to provide validation of the design and characterisation data for a single turbine over the full working λ range. This testing, funded by Marinet 2, was undertaken at the CNR-INM wave-tow tank in Rome, Italy. This allowed for characterisation of the turbine with and without defined waves at controlled speeds with no turbulence present. In addition, testing of the turbine's ability to operate under speed or torque control was conducted.

Stage 2: The single turbine was then tested in the IFREMER wave-current flume facility in Boulogne-Sur-Mer, France, again with and without waves. This allowed for a low turbulence level and a range of flow speeds, again over the full λ range.

Stage 3: With the turbine design validated, the second and third turbines were manufactured and tested in the Kelvin Hydrodynamics Laboratory (KHL) tow tank, in Glasgow.

Table 6 shows an overview of the experimental parameters for each facility. It should be noted that differing pitch angles were used for the IFREMER and KHL cases, this was done to test the effects of differing pitch angles and to understand the repeatability of the pitch angle setting procedure.

Table 6
Table providing an overview of peak non-dimensional quantities observed across the differing test facilities for Turbine 1 (T1).

Qnty	CNR-INM	IFR	KHL
Facility Type	Tow Tank	Flume Tank	Tow Tank
Testing Data	November 2017	April 2018	February 2019
Data Record Length	90s	100s	60s
Facility Dimensions	9 × 3.5 × 220 m	4 × 2 × 14 m	4.6 × 2 × 76 m
Blockage Ratio	2.8 %	8.0 %	6.9 %
Turbine Depth	1.5 m	1 m	1 m
Pitch Angle	8.0°	6.2°	6.2°
Flow/Carriage Velocities	1.00 ms^{-1}	0.50 ms^{-1} 0.60 ms^{-1} 0.90 ms^{-1} 1.00 ms^{-1} 1.05 ms^{-1} 1.10 ms^{-1} 1.20 ms^{-1} 1.30 ms^{-1}	0.80 ms^{-1} 1.0 ms^{-1} 1.2 ms^{-1}

5.1. CNR-INM testing

The Stage 1 tests were undertaken at the CNR-INM wave tank. The tests were conducted by attaching the model HATT to the carriage and towing it along the tank as shown in Fig. 8A. The tests were undertaken to characterise the HATT and to confirm its correct operation. A series of tests were undertaken all with the carriage velocity set to 1 ms^{-1} ($RE_{0.7chord} = 6.48 \times 10^4$). A 0.09 m diameter stanchion held the turbine in place to the tow carriage. The turbine hub centre was set at 1.5 m below the still water surface, and centred in the cross-stream direction. Cables from the turbine were run inside the stanchion to the control and data acquisition systems situated on the carriage. For this set of tests the pitch angle for each blade was set to $8^o \pm 0.5^o$. The tests were undertaken with both speed and torque control over the range of operating λ values. Prior to each test a zero reading was taken to confirm no drift in the instrumentation had occurred.

5.2. IFREMER testing

The Stage 2 test campaign was undertaken at the flume tank facility in Bolougne-Sur-Mer in France. Again a major aspect of this testing was to characterise the turbine performance. In this instance the turbine blades were set to a pitch angle of $6.2^o \pm 0.5^o$. The turbine was supported via the same stanchion arrangement as the CNR-INM testing described in Section 5.1, albeit with different

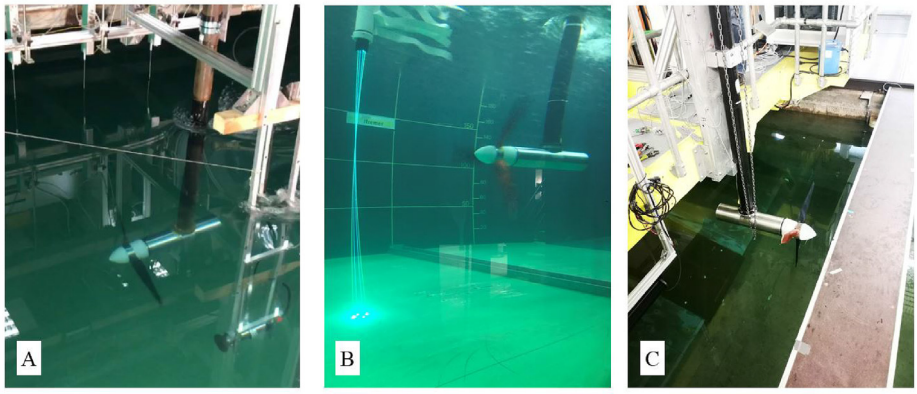

Fig. 8. The test setups at the various testing facilities, A) CNR-INM, B) IFREMER and C) KHL.

supporting bracket arrangement. The setup can be seen in Fig. 8B. The turbine in this case was submerged to a depth of 1 m m and again centralised in the cross stream direction. A Laser Doppler Velocimeter (LDV) was setup to measure the fluid velocity in the stream-wise and cross-stream directions. The measurement volume of the LDV was aligned with the centre of the turbine nose cone, 1 m upstream.

In this instance the turbine was characterised under a variety of fluid velocities ranging between 0.5 ms^{-1} ($RE_{0.7Chord} = 3.25 \times 10^4$) and 1.3 ms^{-1} ($Re_{0.7Chord} = 8.44 \times 10^4$). A honeycomb flow straightener was used at the flow inlet to straighten the flow and reduce the turbulence levels, with prior characterisation of the fluid flow under this set up finding turbulence intensities of approximately 2%. Similarly to the testing undertaken at CNR-INM, both speed and torque control methods were utilised with a variety of rotational velocities and feedback torques applied to test the turbine at a variety of λ values.

5.3. Kelvin Hydrodynamics laboratory testing

Stage 3 testing was undertaken at the Kelvin Hydrodynamic laboratory, the turbine set-up prior to lowering to the 1 m depth can be seen in Fig. 8C. The tests were undertaken to individually characterise the three HATTs, to confirm their correct operation and provide a comparison with each other. An initial series of tests were undertaken for 8 λ settings with carriage speeds of 0.8, 1.0 and 1.2 ms^{-1} ($Re_{0.7Chord} = 5.184 \times 10^4$, 6.48×10^4 and 7.76×10^4 respectively), with speed control. The turbine hub centre was set 1.0 m below the still water surface and centred in the cross-stream direction. Cables, were again, run along the inside of the stanchion from the turbines and connected to the control and data acquisition systems situated on the carriage. For this set of tests the pitch angle for each blade was set to $6.2^o \pm 0.5^o$. On completion of the speed control experiments a series of tests were then completed using torque control. As with all tow tank testing described in this paper prior to each, for each turbine, a zero reading test was undertaken to confirm no drift in the instrumentation had occurred.

5.4. Results

The results section presents the data recorded during the aforementioned testing campaigns with a focus on two aspects: the characterisation of turbine T1 during testing at three differing facilities, Section 5.4.1, and a comparison between the results obtained for each of the three turbines tested at KHL, Section 5.4.2.

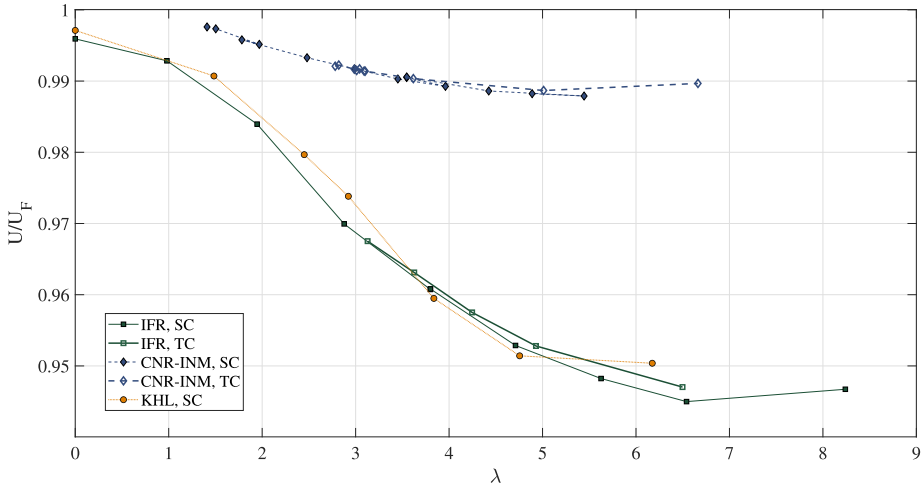

Fig. 9. The blockage ratio of constrained flow to open channel flow velocity, U/U_f, against λ values for the three differing test facilities.

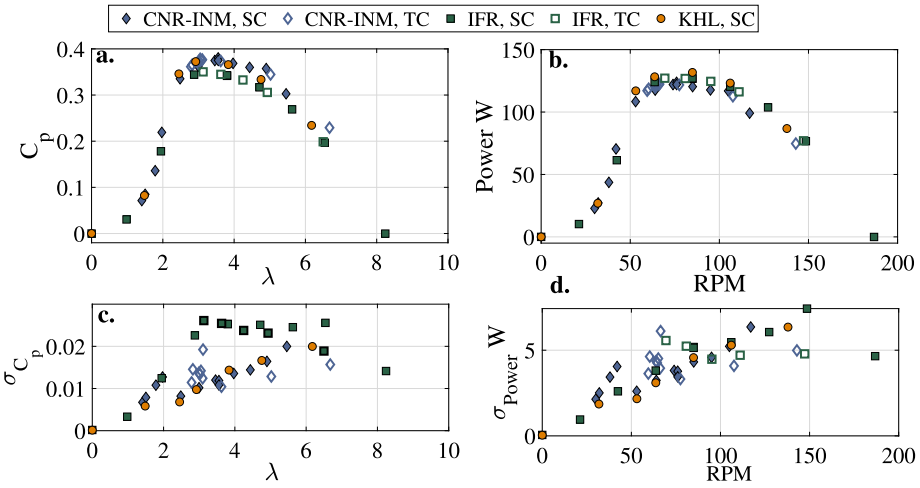

Fig. 10. Blockage corrected power curves obtained whilst testing at CNR-INM,IFREMER and KHL. a) Shows Non-Dimensional power coefficient against λ. b) Shows Power against RPM. c) Shows the standard deviation in non-dimensional power coefficient against λ. d) Shows the standard deviation of power against RPM.

Table 7
Table providing an overview of peak, blockage corrected non-dimensional quantities observed across the differing test facilities for Turbine 1 (T1).

Qnty	CNR-INM	IFR	KHL
Max C_P	0.38	0.35	0.37
λ @ Max C_P	3.55	3.13	2.92
Max C_θ	0.134	0.119	0.141
λ @ Max C_θ	2.5	2.9	2.5
Max C_T	0.86	0.94	0.94
λ @ Max C_T	5.5	6.5	6.2

5.4.1. Single turbine calibrations

Figs. 9 and 10 show a comparison between the results obtained during the CNR-INM, IFREMER and KHL test campaigns for turbine T1 and a flow velocity of 1 ms^{-1}. A comparison was made between the raw and non-dimensional analogues of the power, torque and thrust developed by the turbine. Data for both speed and torque control strategies have also been included for the test campaigns undertaken at both CNR-INM and IFREMER. The non-dimensional coefficients were calculated using equations (1)–(4). Power and torque, along with the non-dimensional equivalents, were calculated for this comparison using the measured PMSM winding currents, as the rotor torque transducer was not available during the CNR-INM testing campaign. The PMSM winding current measurements were decomposed into direct and quadrature axis currents, the quadrature axis currents were then scaled to give the braking torque applied by the PMSM - in this regard it should be noted that these measurements included drive shaft losses. In the cases of the CNR-INM and KHL facilities, the fluid velocity used in the calculations was the carriage velocity. In the case of the IFREMER testing, the fluid velocity used to calculate the non-dimensional power coefficients was the swept-area averaged fluid velocity.

As the differing facilities had differing cross-sectional areas, see Table 6, flow around the turbine would have been constrained and accelerated to differing degrees, resulting in artificially exaggerated turbine performances being recorded. As such, the non-dimensional parameters were corrected to account for the differing blockage ratios in the differing facilities. This was done by estimating the ratio of blockage constrained flow velocity to open channel flow velocity, U/U_f, using the method detailed in Ref. [6]. The ratios developed are plotted in Fig. 9 against λ values for the differing facilities. The aforementioned ratio was squared and cubed before applying as a factor to the non-dimensional thrust and power coefficients, respectively. Table 7 shows the peak non-dimensional values obtained for turbine T1 during the three stages of testing described.

Table 7 shows that relatively good agreement was found in the maximum power, torque and thrust coefficients measured. However, it should be noted that a lower power coefficient was recorded for the IFREMER test cases, as well as discrepancies in the λ values recorded for peak power. Further to this, a slightly lower C_θ value was also recorded for the IFREMER test case. Better agreement was seen in the λ value of peak torque coefficient. A lower value of thrust coefficient was observed, as expected, for the CNR-INM testing. This was likely due to the differing pitch angle setting for the CNR-INM test and helps confirm that in the region of pitch angles varying between 6° and 9° a greater sensitivity in thrust loading is observed in contrast to a relatively invariant power coefficient, as discussed in Section 3.

Inspection of the power curves, in Fig. 10, shows that the IFREMER test cases yielded a generally lower performance curve than the CNR-INM and KHL test cases. Comparison of Fig. 10a and b shows the blockage correction has a significant effect. Whilst the highest power capture was observed for the KHL cases, the blockage correction yields C_P-curves of a similar level for the CNR-INM and KHL cases. The discrepancy between the IFREMER C_P-curve and CNR-INM and KHL C_P-curves is likely to be due to greater drive-train losses during the IFREMER test. A change of dynamic seal between the CNR-INM and IFREMER testing campaigns was undertaken which could explain the deviation. Furthermore, its is also possible that the change in the losses across the differing facilities may have altered the power capture to thrust relationship exploited in the blockage correction approach. This may have led to a distortion in the blockage correction factor applied in the case of the IFREMER tests.

It can be seen in Table 7 that the λ-value associated with maximum power performance varies between facilities - this is likely to be a result of the C_P-curve shape than any inherent difference between the facilities. Explicitly, this is due to the relatively flat shape of the characteristic C_P curve in the peak region as shown in Fig. 10a. This may have been exacerbated by the differing λ values tested for each of the differing test campaigns.

The maximum standard deviation of power and C_P were of the

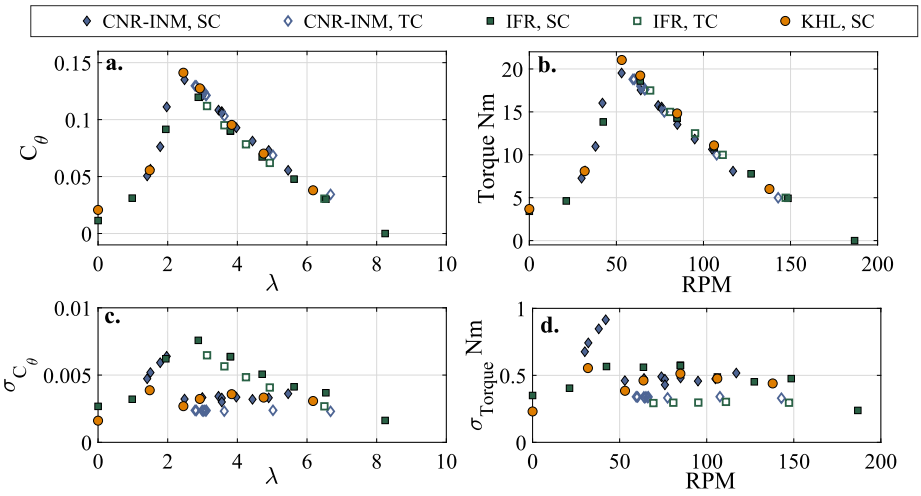

Fig. 11. Blockage Corrected torque curves obtained whilst testing at CNR-INM,IFREMER and KHL. a) Shows Non-Dimensional torque coefficient against λ. b) Shows torque against RPM. c) Shows the standard deviation in non-dimensional torque coefficient against λ. d) Shows the standard deviation in torque against RPM.

order of 3 and 3.5 % of the mean values obtained, respectively. The variability of the power produced by the turbine generally increased with rotational velocity as shown in Fig. 10c and d. The dominant factor in this increase is the nature of how the power is calculated as the product of two measured quantities (PMSM braking torque and rotational velocity), this leads to the product of mean rotor velocity and torque variability becoming dominant in power variability, explaining the dependence on rotor velocity. Similar values for the variability in power and non-dimensional power coefficients were observed for all test cases. Higher variability was expected for the IFREMER test cases due to the presence of turbulence effects in these test cases. This finding would suggest that the variability in power production measured via the motor currents is dominated by measurement noise (common in motor current measurements) and associated PMSM control functions rather than the presence of low level turbulence. Lastly, the effect of torque control rather than speed control seems to have made little difference to the mean and standard deviations which are similar in magnitude for like facilities.

Fig. 11 shows that good agreement was found when comparing the torque measurements from each facility. The blockage correction has had a significant effect on the C_θ curves, which has resulted in very similar C_θ values for the CNR-INM and KHL test campaigns despite lower torsional values being recorded at CNR-INM, as shown by contrasting Fig. 11a and b. It can be seen in Fig. 11a that the slight lower C_θ value, presented in Table 7 for the IFREMER test case arises due to the operating points measured. It can be seen that the measurement points fall either side of peak torque, at $\lambda \approx 2.5$ for the IFREMER test cases - although the shape of the curves observed for all facilities are similar.

The maximum standard deviation of torque and torque coefficients were of the order of 2 and 3 % of the mean values obtained, respectively. It can be seen that variability in torque produced by the rotor is of similar magnitude for each facility for ω-values greater than $\omega = 50$ RPM. Below this value all test cases show an increasing torque variability with increasing ω; the CNR-

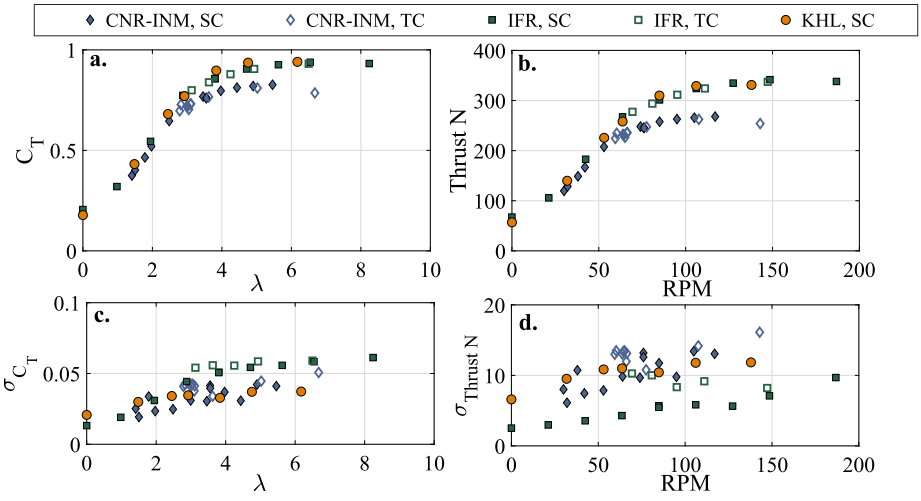

Fig. 12. Blockage corrected thrust curves obtained whilst testing at both CNR-INM and IFREMER. a) Shows Non-Dimensional thrust coefficient against λ. b) Shows thrust against RPM. c) Shows the standard deviation in non-dimensional thrust coefficient against λ. d) Shows the standard deviation in thrust against RPM.

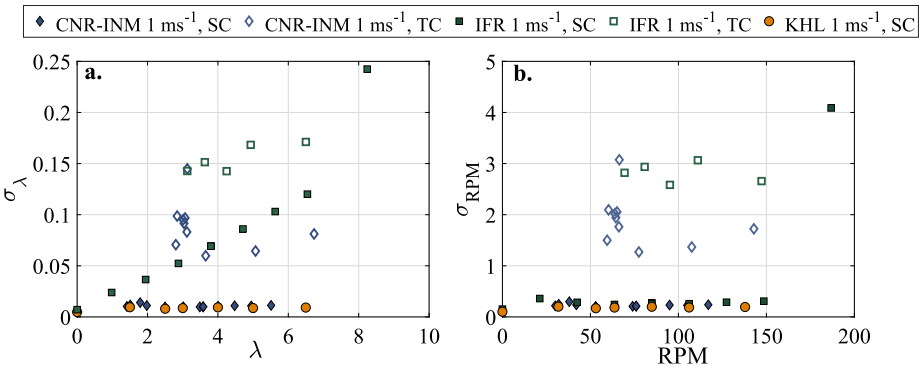

Fig. 13. Figure showing the standard deviation of λ values against λ (left) and the standard deviation of RPM against RPM (right).

INM cases show the most severe torsional variability towards peak torque. In Fig. 11d, it can be seen that the torsional variability was slightly higher for speed control cases than torque control cases, this is reflected in C_θ variability shown in Fig. 11c. It can be seen that the variability in C_θ values measured at IFREMER follows closely the shape of the torque curves developed and shows generally higher variability, especially between $2 < \lambda < 6$. This shows the dependence on the flow velocity variability when calculating σ_{C_θ} via the standard variance propagation equations for independent variables. The similar levels of variability in torque for all speed control cases would suggest, again, that variability related to motor control is dominant over variability observed due to turbulence effects in the flume.

In Fig. 12a and b the differing pitch settings between the CNR-INM tests and the IFREMER and KHL cases are immediately apparent. Both the raw thrust and blockage corrected non-dimensional thrust coefficient curves show excellent agreement for the IFREMER and KHL cases. The C_T vs λ curve for CNR-INM are in agreement with the curves recorded from the other facilities until approximately $\lambda = 3.5$, after this point the curves deviate in shape with the CNR-INM curve becoming concave in shape as a drop-off in thrust is observed at higher λ-values.

Again maximum standard deviation of thrust and thrust coefficients were of the order of 3 and 3.5 % of the median values obtained, respectively. Interesting, the variability in thrust for the tow tank cases measured was found to be higher than those observed in the flume test cases. This unexpected result would suggest that the variability in the thrust loading observed at CNR-INM is driven by a combination of potential tow carriage velocity precision, measurement noise and potential rotor imbalance. This is supported in that relatively similar standard deviations in the thrust coefficient were observed at the IFREMER test facility for similar levels of turbulence and reported in Ref. [27]. Regarding the CNR-INM data, intermittent noise spikes were observed in the thrust data. To combat this additional shielding was added between testing at CNR-INM and IFREMER. Regarding the root causes of the unexpected variability observed at KHL, further analysis will be required to fully understand the unexpected result. Lastly, both thrust and non-dimensional thrust coefficient are affected by the control strategy adopted, exhibiting slightly higher thrust variations under the torque control cases which has been observed previously [19,26].

Fig. 13 shows the standard deviation of the λ-values and RPMs observed at each of the facilities. It is immediately clear that the control strategy has major effect on the variability of the turbine operating point during testing - this is in agreement with the higher thrust and torque fluctuations observed for the torque control case. A discrepancy between the non-dimensional

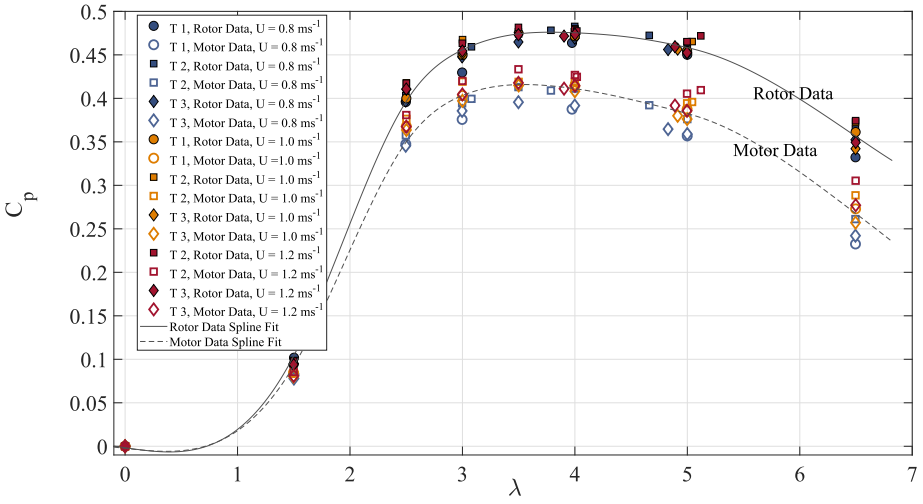

Fig. 14. Characteristic power curves obtained whilst testing at KHL for each of the three turbines, the figures show both the power curves obtained considering rotor transducer measurements and motor power measurements.

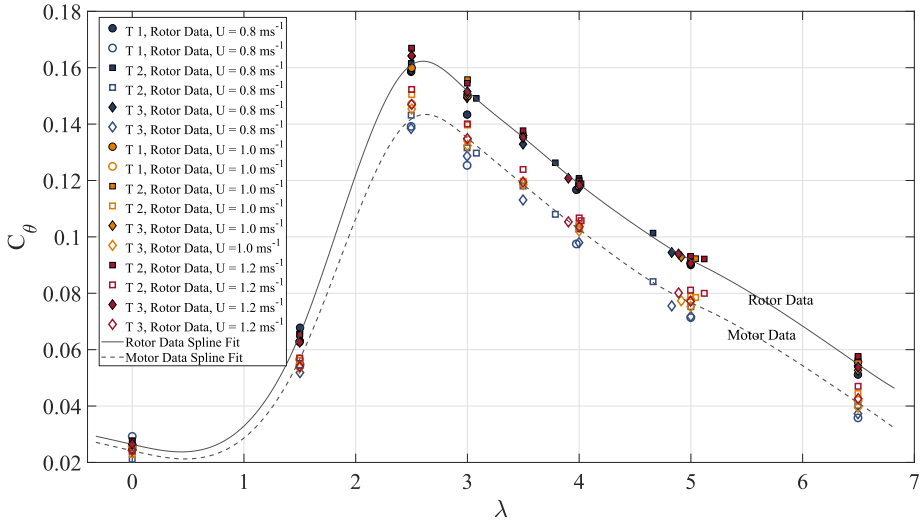

Fig. 15. Characteristic torque curves obtained whilst testing at KHL for each of the three turbines, the figures show both the power curves obtained considering rotor transducer measurements and motor power measurements.

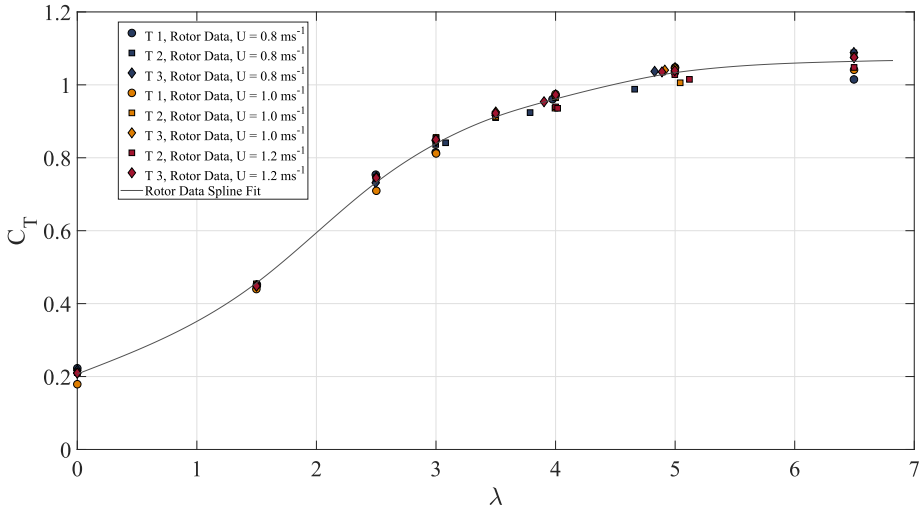

Fig. 16. Characteristic thrust curves obtained whilst testing at KHL for each of the three turbines.

kinematic quantity λ and the RPM standard deviations is exhibited for the IFREMER test case. The increasing trend in standard deviation observed in Fig. 13a would seem to be generated in the variance propagation calculations made. This would suggest that covariance between quantities is significant and should be used in such calculations.

5.4.2. Three turbine characterisation at KHL

Figs. 14 to 18 show the data sets for the three turbines tested at the KHL providing the characteristic curves of C_P, C_θ, C_T, M_x and M_z for the 0.8, 1.0 and 1.2 ms^{-1} carriage velocity cases. The plots are based on the rotor and blade transducer data recorded; in addition C_P and C_θ derived utilising PMSM winding current measurements are also presented, which clearly show the drive train losses. Spline fits to the data have been included for clarity and to highlight the underlying nature of the characteristic curves measured. Table 8 shows the peak quantities observed in the rotor data. Table 8 also shows the maximum standard deviation observed for each non-dimensional quantity at the peak operating point as well as the range of non-dimensional values observed between differing turbines as a percentage of the peak value. The author's note that due to water ingress into the nose cone of T1 during the experiments at KHL, no blade data was captured as such these plots are omitted from Figs. 17 and 18. Furthermore, due to the timing restraints on the testing the water ingress meant it was only possible to test T1 at the 0.8 and 1.0 ms^{-1}. Since this time the cause of the leak has been detected and rectified.

In all cases the non-dimensional characteristics display a very good level of repeatability, not only for each turbine at the separate velocities, but also when comparing each of the differing turbines manufactured. With reference to Fig. 14, the largest spread of C_P values recorded was found at the highest λ-value tested, namely $\lambda = 6.5$. This spread was found to be larger in the C_P values derived from the motor data rather than the rotor transducer. This would suggest, as asserted above, that motor control actions (including winding current measurement noise) generally yield more variable power measurements than the rotor transducer for low turbulence operation. Drive shaft losses, taken as the difference between the motor data derived C_P and the rotor transducer derived C_P, were found to increase with λ and ranged from 11% in the peak power

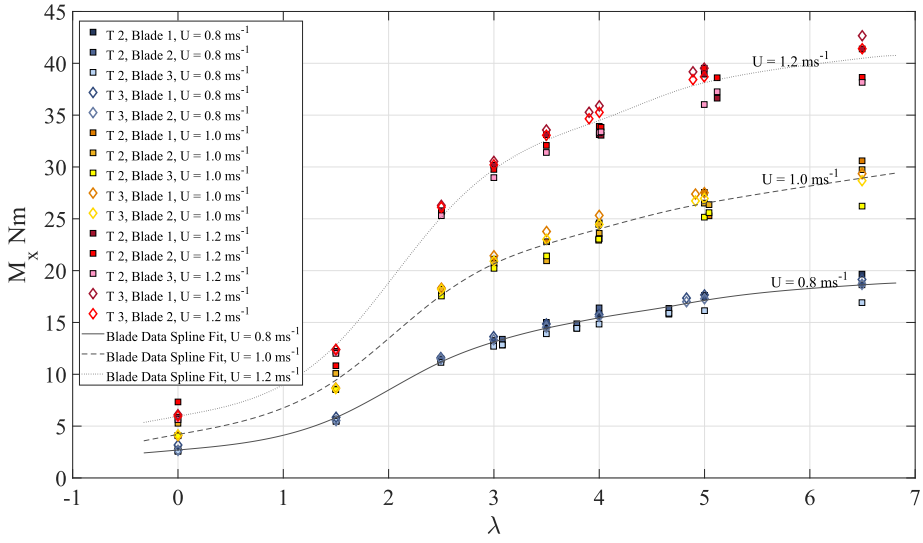

Fig. 17. Characteristic blade root bending moments, flapwise or Mx moments, obtained whilst testing at KHL for each of the three turbines.

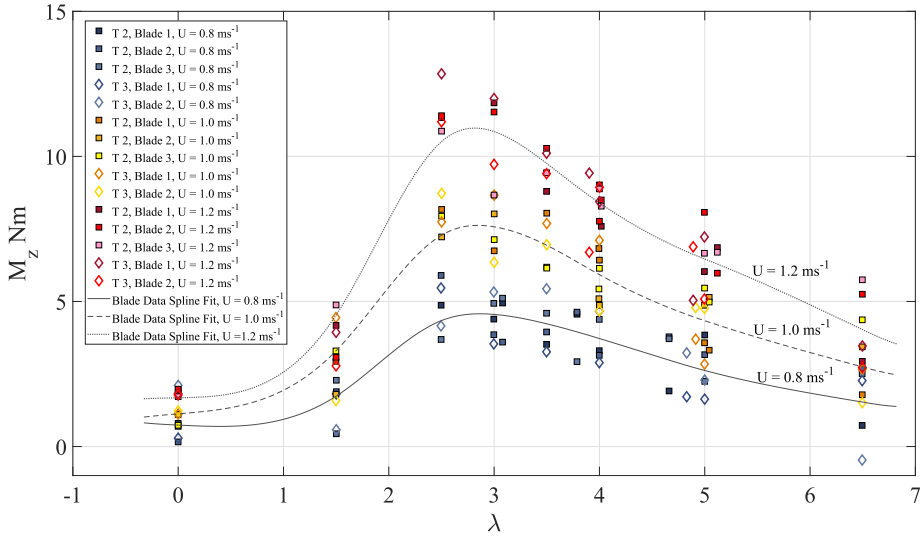

Fig. 18. Characteristic blade root bending moments, edgewise or Mz moments, obtained whilst testing at KHL for each of the three turbines.

region up to 21% at free-wheeling. The losses for all three turbines were consistent, however it was found that slightly higher losses were found for the 0.8 ms^{-1} carriage speed case. Due to these losses, the nature of the C_P curves developed vary between those measured via the motor data and the rotor transducer. Peak C_P derived via the motor data was found to arise at $3 < \lambda < 4$. Whereas the peak power in the rotor transducer data arose at $\lambda = 4$. This distortion of the power curves can be expected as the losses found were not consistent across operating points with aforementioned dependence on rotational velocity.

The non-dimensional torque coefficients observed for the KHL test cases again show good agreement over both differing fluid velocities and for differing turbines, Fig. 15. A peak rotor based C_θ value of 0.16 was found at $\lambda = 2.5$, which coincides with the findings from the other test facilities discussed in Section 5.4.1. Again, the C_θ values calculated via motor current measurements a more widely spread than the rotor transducer based values. Likewise, the motor data based values for the 0.8 ms^{-1} case were generally found to be slightly lower than the other fluid velocity cases. Increased data spread can be observed in the peak torque region as well as the at high λ-values.

Fig. 16 shows very good agreement for the non-dimensional thrust coefficients observed across all test cases. Minimal scatter is observed until a λ value of 6.5, where a maximum C_T of 1.09 was observed. Given the aforementioned sensitivity of the thrust loading experience to blade pitch angle setting, this would suggest high repeatability in blade pitch angle setting.

The individual blade axial moments shown in Fig. 17, show an excellent grouping with each turbine comparable to the other turbines. Fig. 18 shows the M_z moment operating in the rotational direction. There is clearly a wide spread of the data sets both between each blade for the same turbine and also for the additional and identical turbines. What can be extracted from the data sets is that they follow the same trend, as shown in Fig. 15, for the torque loading over the range of λ values, peaking at $\lambda \approx 2.5$ in all cases.

The non-dimensional parameters and blade root bending moment curves have shown that the design and manufacture of the individual turbines is of a quality that allows interchangeability and repeatability. Testing of multiple turbines can be directly compared to the data sets for the individual turbines

Table 8
Table providing an overview of peak non-dimensional quantities observed, with standard deviations for a given turbine presented as well as the range of non-dimensional values recorded across the three turbines.

Qnty	Turbine 1	Turbine 2	Turbine 3
Max C_P	0.47	0.48	0.48
U @ Max C_P	1.0 ms^{-1}	0.8 ms^{-1}	1.0 ms^{-1}
λ @ Max C_P	4	4	4
Max $\sigma_{C_P}@\lambda = 4$	0.013	0.015	0.013
Range $C_P@\lambda = 4$			
% of Max C_P	6.7 %		
Max C_θ	0.16	0.17	0.16
U @ Max C_θ	1.0 ms^{-1}	1.0 ms^{-1}	1.2 ms^{-1}
λ @ Max C_θ	2.5	2.5	2.5
Max $\sigma_{C_\theta}@\lambda = 2.5$	0.003	0.003	0.003
Range $C_\theta@\lambda = 2.5$			
% of Max C_θ	4.2 %		
Max C_T	1.05	1.09	1.09
U @ Max C_T	0.8 ms^{-1}	0.8 ms^{-1}	0.8 ms^{-1}
λ @ Max C_T	5	6.5	6.5
Max $\sigma_{C_T}@\lambda = 6.5$	0.05	0.02	0.02
Range $C_\theta@\lambda = 2.5$			
% of Max C_T	6.8 %		

providing high levels of confidence and reliability. The introduction of turbulence, wakes, wave-current interaction, current-structural interaction or in fact any combination can be directly compared to these data sets to determine their influence of the dynamic loading of the turbines.

5.5. Discussion

The results section presents the data relating to a variety of test campaigns for a single turbine, namely T1, followed by a comparison of the non-dimensional parameters of the three turbines manufactured to the specifications detailed throughout the paper.

The comparison of the findings from the differing test campaigns shows that relatively repeatable results were generated. However, some significant differences were highlighted between the findings. The authors note that this was not entirely unexpected as these tests were performed at differing stages of development and design integration for the prototype turbine, turbine T1. These results, in terms of power and torque, were generated by utilising PMSM winding current measurements. The relatively large spread in the data and the deviation of the power curve recorded at IFREMER relative to the tow tank cases, suggests that detailed understanding and characterisation of motor control operations and drive shaft losses are required to generate concrete findings when using motor current data to measure rotor power and torque. Furthermore, it was considered that changes in the turbine set-up during development are likely to have changed the drive train losses characterisation - this may have impacted on the blockage correction method utilised by changing the power to thrust relationship of the turbine.

Another aspect of deviation between the test cases was the differing thrust characteristics observed during the testing undertaken at CNR-INM relative to the latter test cases. This was largely attributed to the differing pitch angle settings tested at CNR-INM relative to the test campaigns undertaken at IFREMER and KHL. The differing pitch angle settings were tested to confirm the relative insensitivity to pitch angle variations between 6^o and 9^o of the power produced. The inverse finding for rotor thrust was also found, as expected based on the BEMT and CFD modelling. Whilst the finding of the modelling stages seem to have been confirmed, the authors believe a structured test campaign is required to fully quantify the effects of pitch angle on power and thrust production.

The variability observed between facilities was of a similar magnitude which was unexpected due to the presence of approximately 2 % turbulence intensity experienced at IFREMER. This highlights the requirement for high levels of electrical shielding, a high degree of accuracy in rotor and drive train set-up and the requirement to measure rotor quantities directly. This finding is non-trivial in the quantification of dynamic loading and suggested that before undertaking more ambitious test campaigns including unsteady effects, such as testing under wave conditions and high levels of turbulence, an initial set of steady-state tests at the given facility should be undertaken as a benchmark.

Lastly, the mean non-dimensional quantities observed at the KHL facility for all three of the manufactured turbines showed good agreement. As such, there is a high level certainty in the turbine characterisations performed. Relatively large scatter was found for the blade root bending moment measurements taken. These results suggest that improved amplification and filtering of the blade root bending moment measurements maybe required, although it cannot be concluded at this stage that the differing quantities observed are spurious findings.

5.6. Conclusions and further work

The paper presents the specification of a 1/20th scale HATT design, detailing blade design activities as well as measurement and turbine control processes. The paper then outlines testing of the three lab scale HATTs.

The updated blade design yielded higher turbine performance with a relatively minor increase in thrust loading. A maximum C_P of 0.47 at $\lambda = 4$ was observed with a maximum C_T of 1.09 found for λ values above 6.5. Free-wheeling occurred at $\lambda = 8$, with peak torque at $\lambda = 2.5$.

The operation and design of the turbine and its instrumentation was demonstrated across the various test campaigns. Under speed control the standard deviation of the rotational velocity of the turbine was, in most cases, below 0.3 RPM, other than at free-wheeling. Under torque control torsional variations of 0.4 Nm were observed. The quantities represent variability of less than 2.5 % relative to median values and demonstrated a high degree of stability in the turbine control systems across all operating ranges.

Good agreement between the tests undertaken at differing facilities was found given the development and maintenance of the turbine between test campaigns. It was found that using motor current measurements to estimate turbine rotor torque and power can lead to uncertainty in results if a high degree of characterisation of motor control variability and drive shaft losses are not undertaken. Furthermore, it was found that it is not clear the effect of drive shaft losses on the blockage correction approach which will change the power to thrust characteristics for the turbine. A high degree of repeatability of the rotor quantities across all three turbines was confirmed via the test campaign undertaken at the KHL.

Further work is being undertaken to generate an in-depth characterisation of the three turbines tested at the KHL. This work will seek to understand in more detail the dynamic aspects associated with the turbine operation and the discrepancies between the turbines in this regard. The blade root bending moment instrumentation will be further developed with greater amplification and filtering to improve measurement consistency. Lastly, the three turbines have been tested in a variety of dynamic conditions, the findings relating to these campaigns will be presented in future. Furthermore, the turbines detailed have been utilised for array characterisation at FloWave, Edinburgh and will be used for detailed flow characterisation of two interacting turbines, with this test campaign being undertaken at IFREMER.

Declaration of competing interest

The authors declare that they have no known competing financial interests or personal relationships that could have appeared to influence the work reported in this paper.

CRediT authorship contribution statement

Matthew Allmark: Methodology, Software, Validation, Formal analysis, Investigation, Resources, Data curation, Writing - original draft, Writing - review & editing, Visualization, Funding acquisition. **Robert Ellis:** Software, Investigation. **Catherine Lloyd:** Investigation. **Stephanie Ordonez-Sanchez:** Methodology, Software, Validation, Investigation, Writing - review & editing. **Kate Johannesen:** Methodology. **Carl Byrne:** Resources. **Cameron Johnstone:** Supervision, Project administration, Funding acquisition. **Tim O'Doherty:** Resources, Writing - review & editing, Supervision, Project administration, Funding acquisition. **Allan Mason-Jones:** Investigation.

Acknowledgements

Funding: This work was supported by the Engineering and Physical Sciences Research Council [DyLoTTA –EP/N020782/1]; Horizon2020 [MARINET2-731084]; Engineering and Physical Sciences Research Council[Cardiff University Impact Acceleration Account-EP/R51150X/1].

Appendix A. Consideration of Reynolds Effects

To confirm the comparisons made in Sections 5.4.1 and 5.4.2 were not subject to Reynolds effects, a comparison of non-dimensional quantities for tests undertaken at differing flow speeds and associated chord based Reynold's numbers undertaken at IFREMER were considered. Figure A.19 shows the non-dimensional power coefficient distribution for differing chord based Reynolds numbers. Here the chord based Reynolds number is defined as:

$$RE_{0.7Chord} = \frac{\rho \cdot C_{0.7} \cdot U}{\mu} \quad (A.1)$$

where, ρ is the fluid density in kgm^{-3}, $C_{0.7}$ is the chord length at 70 % of the radius in m, U is the mean fluid velocity in ms^{-1} and μ is the dynamic viscosity in $Pa \cdot s$. Figure A.19 shows that Reynolds effects become negligible, with a variation of 1 %, for Reynold's numbers above $RE_{0.7Chord} = 6.48E+4$.

Appendix B. Instrumentation Calibration

Appendix B.0.1. Rotor Thrust and Torque Transducer Calibrations

The rotor thrust and torque transducers were calibrated by applied measurements. Calibration certificates were provided with the transducers detailing the calibrations undertaken and reporting on non-linearity, hysteresis and cross-axis sensitivity.

Table B9
Summary of calibration results for the 3 torque thrust transducers as undertaken by Applied Measurements Ltd.

Qnty	Turbine 1	Turbine 2	Turbine 3
Serial No.	54283	54284	157961
Thrust Gradient, A/N	5.308E-3	5.349E-3	5.333E-3
Thrust non-linearity	±0.043% FS	±0.056% FS	±0.043% FS
Thrust hysteresis	<0.074% FS	<0.098% FS	<0.074% FS
Thrust cross-sensitivity	<0.23% FS	<0.45% FS	<0.23% FS
Torque Gradient, A/Nm	8.00E-2	8.01E-2	8.00E-2
Torque non-linearity	±0.031% FS	±0.031% FS	±0.031% FS
Torque hysteresis	<0.075% FS	<0.062% FS	<0.075% FS
Torque cross-sensitivity	<0.35% FS	<0.18% FS	<0.35% FS

Appendix B.0.2. Flap-Wise Blade Root Bending Moment Calibrations

The three flap-wise blade root bending moment transducers for each turbine were calibrated according to the BSI - standard [28]. Increasing moments were applied to the transducers and the current output from the amplifiers were recorded in Amps. The weights used to create the moments had an uncertainty of 0.001g with the distance over which the load was applied had an uncertainty of 0.1 mm. Figures B.20 and B.21 show the calibration and residuals associated with the linear fit for hub 1, blade 2. Tables B.10 to B.12 show the gradients and uncertainties for each of the calibrated transducers.

Table B10
Summary of calibration results for flap-wise blade root bending moment transducers, Turbine 1.

Qnty	Blade 1	Blade 2	Blade 3
Gradient A/Nm	1.59E-4	1.62E-4	1.57E-4
Fit Uncertainty (SEE), Nm	0.62	0.45	0.44
Bias Uncertainty, Nm	0.12	0.12	0.12
Total Uncertainty, Nm	0.63	0.47	0.46

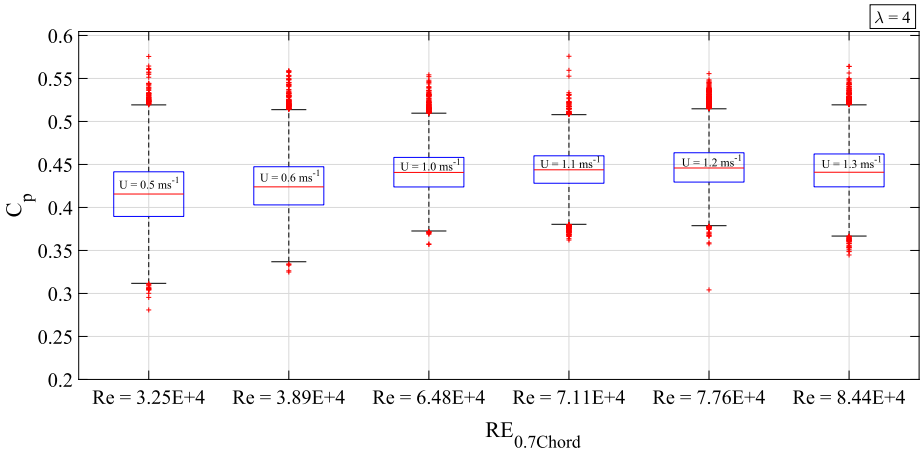

Fig. A19. Comparison of C_P values observed for tests under taken at differing fluid velocities. The C_P values are plotted against chord length based Reynold's Number for a fixed λ-value of $\lambda = 4$.

Table B11
Summary of calibration results for flap-wise blade root bending moment transducers, Turbine 2.

Qnty	Blade 1	Blade 2	Blade 3
Gradient A/Nm	1.60E-4	1.63E-4	1.62E-4
Fit Uncertainty (SEE), Nm	0.43	0.41	0.90
Bias Uncertainty, Nm	0.12	0.12	0.12
Total Uncertainty, Nm	0.45	0.43	0.90

Table B12
Summary of calibration results for flap-wise blade root bending moment transducers, Turbine 3.

Qnty	Blade 1	Blade 2	Blade 3
Gradient A/Nm	1.60E-4	1.62E-4	NA
Fit Uncertainty (SEE), Nm	0.41	0.42	NA
Bias Uncertainty, Nm	0.12	0.12	NA
Total Uncertainty, Nm	0.43	0.44	NA

Appendix B.0.3. Edge-Wise Blade Root Bending Moment Calibrations

The edge-wise blade root bending moment calibrations were undertaken in-situ comparing the outputs from the blade root bending moment transducers with the outputs from the calibrated rotor torque transducer. In this way the relationship in Equation (B.1) was assumed to hold for mean quantities. Furthermore, it was assumed that the mean edge-wise bending moment from each blade was equal for a given test. This method gave relatively good results, however large uncertainties were found and can be seen in the spread of data in Fig. 18. Improved calibrations for this measurement are being undertaken for subsequent test campaigns.

$$\overline{\tau}_{rotor} = \sum_{i=1}^{3} M_{zi} \tag{B1}$$

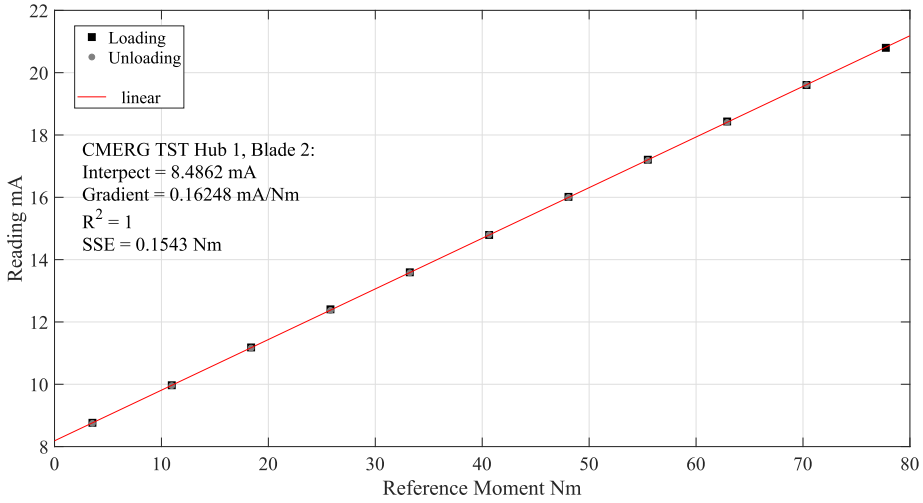

Fig. B20. The calibration results for the flapwise blade root bending moment transducer for blade 2, hub 1.

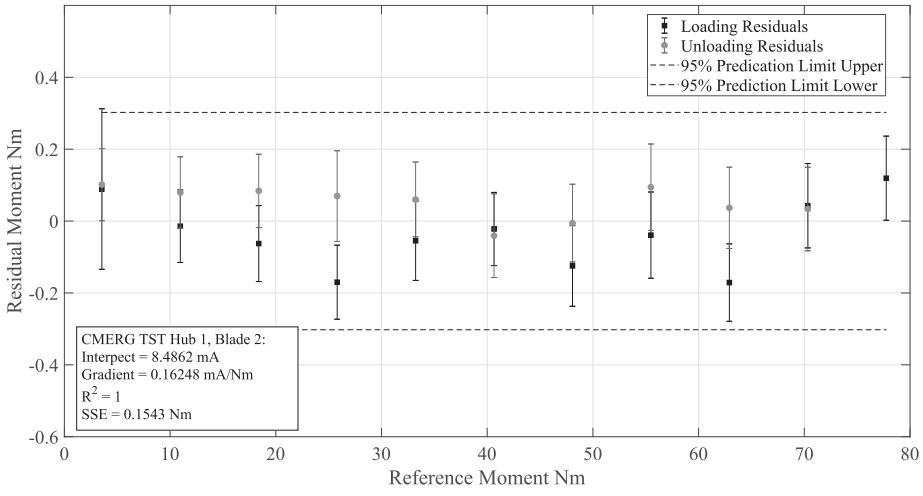

Fig. B21. Fitted residuals for calibration results for the flapwise blade root bending moment transducer for blade 2, hub 1.

References

[1] Department of Energy & Climate Change, DECC Electricity Generation Costs 2013 - GOV.UK, Tech. Rep., Department of Energy & Climate Change, London, 2013. URL, https://www.gov.uk/government/publications/decc-electricity-generation-costs-2013.

[2] X.-P. Zhang, P. Zeng, Marine energy technology [Scanning the issue], Proc. IEEE 101 (4) (2013) 862–865, https://doi.org/10.1109/JPROC.2013.2244735.

[3] European Parliament, Directive (EU) 2018/2001 of the European Parliament and of the Council of 11 December 2018 on the Promotion of the Use of Energy from Renewable Sources, Tech. Rep, European Parliament and Council of 11 December 2018, London, 2018. URL, https://eur-lex.europa.eu/legal-content/EN/ALL/?uri=uriserv:OJ.L_.2018.328.01.0082.01.ENG.

[4] C. Johnstone, D. Pratt, J. Clarke, A. Grant, A techno-economic analysis of tidal energy technology, Renew. Energy 49 (2013) 101–106, https://doi.org/10.1016/J.RENENE.2012.01.054.

[5] Iec, Iec 61400 - wind turbines, Tech. rep., IEC (2015). URL, https://webstore.iec.ch/publication/22259.

[6] A. Bahaj, A. Molland, J. Chaplin, W. Batten, Power and thrust measurements of marine current turbines under various hydrodynamic flow conditions in a cavitation tunnel and a towing tank, Renew. Energy 32 (3) (2007) 407–426, https://doi.org/10.1016/J.RENENE.2006.01.012.

[7] J.A. Clarke, G. Connor, A.D. Grant, C.M. Johnstone, Design and testing of a contra-rotating tidal current turbine, Proc. IME J. Power Energy 221 (2) (2007) 171–179, https://doi.org/10.1243/09576509JPE296.

[8] T. Stallard, R. Collings, T. Feng, J. Whelan, Interactions between tidal turbine wakes: experimental study of a group of three-bladed rotors, Phil. Trans. Math. Phys. Eng. Sci. 371 (1985) (2013), https://doi.org/10.1098/rsta.2012.0159, 20120159–20120159.

[9] P. Mycek, B. Gaurier, G. Germain, G. Pinon, E. Rivoalen, Numerical and experimental study of the interaction between two marine current turbines, Int. J. Mar. Energy 1 (2013) 70–83, https://doi.org/10.1016/j.ijome.2013.05.007.

[10] P. Mycek, B. Gaurier, G. Germain, G. Pinon, E. Rivoalen, Experimental study of the turbulence intensity effects on marine current turbines behaviour. Part II: two interacting turbines, Renew. Energy 68 (2014) 876–892, https://doi.org/10.1016/J.RENENE.2013.12.048.

[11] P. Mycek, B. Gaurier, G. Germain, G. Pinon, E. Rivoalen, Experimental study of the turbulence intensity effects on marine current turbines behaviour. Part I: one single turbine, Renew. Energy 66 (2014) 729–746, https://doi.org/10.1016/J.RENENE.2013.12.036.

[12] G.S. Payne, T. Stallard, R. Martinez, Design and manufacture of a bed supported tidal turbine model for blade and shaft load measurement in turbulent flow and waves, Renew. Energy 107 (2017) 312–326, https://doi.org/10.1016/J.RENENE.2017.01.068.

[13] A. Mason-Jones, Performance Assessment of a Horizontal Axis Tidal Turbine in a High Velocity Shear Environment, Ph.D. thesis, Cardiff University, 2010.

[14] M.J. Allmark, Condition Monitoring and Fault Diagnosis of Tidal Stream Turbines Subjected to Rotor Imbalance Faults, Ph.D. thesis, Cardiff University, 2016.

[15] C. Frost, C.E. Morris, A. Mason-Jones, D.M. O'Doherty, T. O'Doherty, The effect of tidal flow directionality on tidal turbine performance characteristics, Renew. Energy 78 (2015) 609–620, https://doi.org/10.1016/j.renene.2015.01.053.

[16] C. Morris, Influence of Solidity on the Performance, Swirl Characteristics, Wake Recovery and Blade Deflection of a Horizontal axis Tidal Turbine, Ph.D. thesis, Cardiff University, 2014.

[17] M. Allmark, R. Grosvenor, P. Prickett, An approach to the characterisation of the performance of a tidal stream turbine, Renew. Energy 111 (2017) 849–860, https://doi.org/10.1016/j.renene.2017.05.010. URL, http://linkinghub.elsevier.com/retrieve/pii/S0960148117303956.

[18] S. Ordonez-Sanchez, R. Ellis, K. Porter, M. Allmark, T. O'Doherty, A. Mason-Jones, C. Johnstone, Numerical models to predict the performance of tidal stream turbines working under off-design conditions, Ocean. Eng. 181 (2019) 198–211, https://doi.org/10.1016/J.OCEANENG.2019.04.027. URL, https://www.sciencedirect.com/science/article/pii/S0029801818312848.

[19] S. Ordonez Sanchez, K. Porter, C. Frost, M. Allmark, C. Johnstone, T. O'Doherty, Effects of extreme wave-current interactions on the performance of tidal stream turbines, in: 3rd Asian Wave and Tidal Energy Conferenece, Singapore, 2016.

[20] A. Mason-Jones, D. O'Doherty, C. Morris, T. O'Doherty, C. Byrne, P. Prickett, R. Grosvenor, I. Owen, S. Tedds, R. Poole, Non-dimensional scaling of tidal stream turbines, Energy 44 (1) (2012) 820–829, https://doi.org/10.1016/J.ENERGY.2012.05.010.

[21] D. Egarr, T. O'doherty, S. Morris, R. Ayre, Feasibility study using computational fluid dynamics for the use of a turbine for extracting energy from the tide, in: 15th Australasian Fluid Mechanics Conference, 2004, https://doi.org/10.13140/2.1.4852.3041.

[22] T. Nevalainen, C. Johnstone, A. Grant, A sensitivity analysis on tidal stream turbine loads caused by operational, geometric design and inflow parameters, Int. J. Mar. Energy 16 (2016) 51–64, https://doi.org/10.1016/J.IJOME.2016.05.005.

[23] R. Ellis, M. Allmark, T. O'Doherty, A. Mason-Jones, S. Ordonez-Sanchez, K. Johannesen, C. Johnstone, Design process for a scale horizontal axis tidal turbine blade, in: 4th Asian Wave and Tidal Energy Conference, Taipei, 2018.

[24] F.R. Menter, A comparison of some recent eddy-viscosity turbulence models, J. Fluids Eng. Trans. ASME 118 (3) (1996) 514–519, https://doi.org/10.1115/1.2817788.

[25] S.A. El-Shahat, G. Li, F. Lai, L. Fu, Investigation of parameters affecting horizontal axis tidal current turbines modeling by blade element momentum theory, Ocean. Eng. 202 (2020) 107176, https://doi.org/10.1016/j.oceaneng.2020.107176.

[26] S. Ordonez-Sanchez, M. Allmark, K. Porter, R. Ellis, C. Lloyd, I. Santic, T. O'Doherty, C. Johnstone, Analysis of a horizontal-Axis tidal turbine performance in the presence of regular and irregular waves using two control strategies, Energies 12 (3) (2019) 367, https://doi.org/10.3390/en12030367. URL, http://www.mdpi.com/1996-1073/12/3/367.

[27] B. Gaurier, G. Germain, J. Facq, C. Johnstone, A. Grant, A. Day, E. Nixon, F. Di Felice, M. Costanzo, Tidal energy "Round Robin" tests comparisons between towing tank and circulating tank results, Int. J. Mar. Energy 12 (2015) 87–109, https://doi.org/10.1016/J.IJOME.2015.05.005. URL, https://www.sciencedirect.com/science/article/pii/S2214166915000223.

[28] BS 8422:2003, Force measurement. Strain gauge load cell systems. Calibration method, Tech. rep., BSI (2003), 0 580 42746 3. URL, https://shop.bsigroup.com/ProductDetail/?pid=000000000030067617.